Numerical Simulation of Microstructured Semiconductor Devices, Transducers, and Systems

St. Dürndorfer, V. Gradinaru, Ronald H. W. Hoppe, E.-R. König, G. Schrag, Gerhard Wachutka

Angaben zur Veröffentlichung / Publication details:

Dürndorfer, St., V. Gradinaru, Ronald H. W. Hoppe, E.-R. König, G. Schrag, and Gerhard Wachutka. 1999. "Numerical Simulation of Microstructured Semiconductor Devices, Transducers, and Systems." *Lecture Notes in Computational Science and Engineering* 8: 309–23. https://doi.org/10.1007/978-3-642-60155-2_26.

Numerical Simulation of Microstructured Semiconductor Devices, Transducers, and Systems

St. Dürndorfer[1], V. Gradinaru[1], R.H.W. Hoppe[1], E.-R. König[2], G. Schrag[2], and G. Wachutka[2]

[1] Inst. of Mathematics, University of Augsburg, 86135 Augsburg, Germany
[2] Chair of Physics of Electrotechn., Techn. University of Munich, 80333 Munich, Germany

Abstract The numerical simulation of microstructured semiconductor devices, transducers, and systems aiming at an optimal layout and design often has to take into account that the operating behaviour is based on the interaction of various physical phenomena. This requires on one hand the simulation to be based on a consistent, tailored modeling of the underlying physical processes and on the other hand the use of modern methods in the numerical solution of PDEs and systems thereof such as efficient iterative solvers and adaptive grid refinement and coarsening. In this contribution, the development and implementation of such techniques will be outlined for three industrially relevant case studies.
The first one is concerned with the minimization of parasitic effects in converter modules used in high power electronics which amounts to the solution of a shape and topology optimization problem. Here, we consider the efficient computation of electromagnetic potentials related to Maxwell's equations based on a discretization in terms of curl-conforming edge elements.
The second problem deals with electrostatically driven micromembrane pumps that are intended to be used in medical sciences to control metabolism or in the chemical analysis of freshwater bodies. In particular, we will address the simulation of the electromechanical coupling that characterizes the operating behaviour of the electrostatic drive and the fluid-structure interaction between the fluid flow and the deformation of the passive valves.
Finally, we consider the computation of the temperature and heat flow distribution in micromachined deformable mirrors that can be used for the positioning of laser beams in optical eye surgery. Emphasis will be laid on a combined time-step selection and adaptivity in space for a primal mixed discretization of the underlying heat equation.

1 Computation of Parasitic Inductivities in High Power Electronic Devices

As an example for a high power electronic device we consider a converter module used, e.g., as an electric drive for high power electric motors.

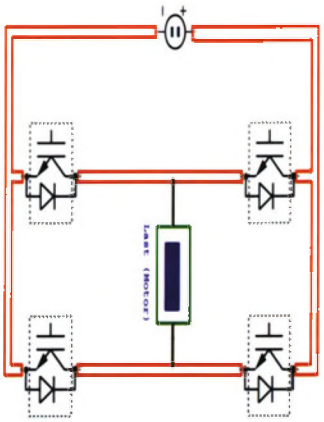

Fig. 1.1a. Converter module

Fig. 1.1b. Geometry of a bus bar

Fig.1.1a shows the schematic representation of such a converter module transforming direct current into alternating current. The module consists of specific semiconductor devices (IGBTs (Insulated Gate Bipolar Transistors)) serving as valves for the electric current that are connected with the motor to be driven by conducting bus bars. Fig. 1.1b displays the geometric structure of such a bus bar.

Since the use of high voltages is intended (several 100 kV) and the switching time of the IGBTs are small ($\tau_{\text{switch}} \sim 100$ ns), undesirable side effects occur such as induced voltage peaks, parasitic inductivities caused by eddy currents, and local overheating. In particular, the parasitic inductivities typically lead to power losses. Therefore, the objective is to design the bus bars and the overall configuration of the converter module in such a way that the total inductivity is minimized.
Considering a converter module that consists of N conducting bars Ω_ν , $1 \leq \nu \leq N$, each bar containing N_ν contacts $T_{\nu\alpha}$, $1 \leq \alpha \leq N_\nu$, the total inductivity with respect to the time horizon $[0,T]$ is given by

$$L_{\text{tot}} := \left(\sum_{\nu,\alpha} \sum_{\mu,\beta} \int_0^T | L_{\nu\alpha,\mu\beta}(t) |^2 \, dt \right)^{1/2} \tag{1}$$

where $L_{\nu\alpha,\mu\beta}(t)$ stands for the generalized transient inductivity coefficient

$$L_{\nu\alpha,\mu\beta}(t) := \frac{1}{\sigma} \int_{\Omega_\nu} \mathbf{J}_{\nu\alpha}(x) \cdot \mathbf{S}(t) \mathbf{J}_{\mu\beta}(x) \, dx \quad .$$

Here, $\mathbf{J}_{\nu\alpha}$ denotes the current associated with the bus bar Ω_ν at contact $T_{\nu\alpha}$ and $\mathbf{S}(\cdot)$ refers to the solution operator of the equation associated with the

magnetic vector potential (cf. (1.5) below).
In particular, introducing an electric potential φ and a magnetic vector potential $\mathbf{A}$ according to

$$\mathbf{E} \;=\; -\mathrm{grad}\,\varphi \;-\; \frac{\partial\,\mathbf{A}}{\partial\,t} \quad , \quad \mathbf{B} \;=\; \mathrm{curl}\,\mathbf{A} \;,$$

Maxwell's equations give rise to the coupled system

$$\frac{\epsilon}{\sigma}\,\frac{\partial^2\,\mathbf{A}}{\partial\,t^2} \;+\; \mu\sigma\,\frac{\partial\,\mathbf{A}}{\partial\,t} \;+\; \mathrm{curl\,curl}\,\mathbf{A} \;=\; -\frac{\epsilon}{\sigma}\,\mathrm{grad}\,\frac{\partial\,\varphi}{\partial\,t} \;-\; \mathrm{grad}\,\varphi \;, \tag{2}$$

$$\mathrm{div}\,(\mathrm{grad}\,\varphi \;+\; \frac{\epsilon}{\sigma}\,\mathrm{grad}\,\frac{\partial\,\varphi}{\partial\,t}) \;+\; \mathrm{div}\,(\frac{\partial\,\mathbf{A}}{\partial\,t} \;+\; \frac{\epsilon}{\sigma}\,\frac{\partial^2\,\mathbf{A}}{\partial\,t^2}) \;=\; 0 \;. \tag{3}$$

We decouple the potentials by the Coulomb-gauge $\mathrm{div}\,\mathbf{A} = 0$ and perform a separation of time-scales observing that the dielectric time constant $\frac{\varepsilon}{\sigma}$ (ratio of the electric permittivity and conductivity) is much smaller than the switching time τ_{switch}. In other words, there are no electromagnetic waves and the corresponding terms in (1.2) and (1.3) can be neglected. We thus end up with the reduced model equations

$$\mathrm{div}\,(\sigma\,\mathrm{grad}\,\varphi) \;=\; 0 \;\text{ in }\; \Omega \;,\; \sigma\,\mathbf{n}\cdot\mathrm{grad}\,\varphi \;=\; \begin{cases} -I_{\nu\alpha}(t) & \text{on}\, T_{\nu\alpha} \\ 0 & \text{else} \end{cases} \;, \tag{4}$$

$$\frac{\partial\,\mathbf{A}}{\partial\,t} \;+\; \frac{1}{\mu\sigma}\,\mathrm{curl\,curl}\,\mathbf{A} = \begin{cases} \frac{1}{\sigma}\,\mathbf{J}_{\nu\alpha} & \text{in } \Omega \\ 0 & \text{in } \mathbf{R}^3 \setminus \Omega \end{cases} \tag{5}$$

where (1.5) has to be completed by appropriate boundary conditions on $\Gamma = \partial\Omega$ and a Sommerfeld radiation condition in case of the exterior domain problem.
For the numerical solution of the interior domain problem we discretize (1.5) implicitly in time by means of the backward Euler scheme and use Nédélec's curl-conforming edge elements (cf., e.g., [10]) for discretization in space which is based on the variational formulation of the semi-discretized problem:
Find $\mathbf{A}^m \in H_0(\mathbf{curl};\Omega) \;:=\; \{\mathbf{Q} \in L^2(\Omega)^3 \;|\; \mathbf{curl}\,\mathbf{Q} \in L^2(\Omega)^3 \;,\; \mathbf{n}\wedge\mathbf{Q}\,|_\Gamma = 0\}$ such that

$$a(\mathbf{A}^m,\mathbf{Q}) \;=\; (\mathbf{F}^m,\mathbf{Q})_{0;\Omega} \quad , \quad \mathbf{Q} \in H_0(\mathbf{curl};\Omega) \tag{6}$$

where

$$a(\mathbf{A}^m,\mathbf{Q}) \;:=\; (\mathbf{curl}\,\mathbf{A}^m,\mathbf{curl}\,\mathbf{Q})_{0;\Omega} \;+\; \alpha\,(\mathbf{A}^m,\mathbf{Q})_{0;\Omega} \;,$$

$(\cdot,\cdot)_{0;\Omega}$ stands for the standard L^2-inner product and
$\mathbf{F}^m := \mu\,\mathbf{J}_{\nu\alpha} - (\Delta t)^{-1}\mathbf{A}^{m-1}$,
$\alpha := (\Delta t)^{-1}\mu\sigma \;,\; \Delta t := t^m - t^{m-1} \;,\; m \in \mathbf{N}$.
In particular, given a simplicial triangulation $\mathcal{T}_h$ of Ω, the lowest order curl-conforming finite element space is given by

$$Nd_1(\Omega;\mathcal{T}_h) \;:=\; \{\mathbf{Q} \in H(\mathrm{curl};\Omega) \mid \mathbf{Q}\,|_T \in Nd_1(T) \;,\; T \in \mathcal{T}_h\}$$

where $Nd_1(T)$, $T \in \mathcal{T}_h$, are Nédélec's edge elements

$$Nd_1(T) \;:=\; \{\, \mathbf{Q} \;=\; \mathbf{a} \;+\; \mathbf{b} \wedge \mathbf{x} \;\mid\; \mathbf{a}, \mathbf{b} \in P_0(T)^3 \,\} \quad , \quad T \in \mathcal{T}_h \;\; .$$

Note that any vector field $\mathbf{Q} \in Nd_1(T)$ is uniquely determined by six degrees of freedom given in terms of the zero order moments of the tangential components with respect to the six edges E of the element

$$\ell(\mathbf{Q}) \;:=\; \int\limits_E \mathbf{t}_E \cdot \mathbf{Q} \, d\sigma \;\; .$$

Setting $Nd_{1,0}(\Omega; \mathcal{T}_h) := \{\mathbf{Q}_h \in Nd_1(\Omega; \mathcal{T}_h) \mid \mathbf{n} \wedge \mathbf{Q}_h \mid_\Gamma = 0\}$, the fully discretized problem amounts to the computation of a vector field in $Nd_{1,0}(\Omega; \mathcal{T}_h)$ such that

$$a(\mathbf{A}_h, \mathbf{Q}_h) \;=\; (\mathbf{F}, \mathbf{Q}_h)_{0;\Omega} \quad , \quad \mathbf{Q}_h \in Nd_{1,0}(\Omega; \mathcal{T}_h) \tag{7}$$

where for notational convenience we have dropped the upper index m indicating the respective time level.
For the efficient numerical solution of (1.7) we use an adaptive multilevel iterative scheme whose characteristic feature is a multigrid algorithm with respect to an adaptively generated hierarchy $(\mathcal{T}_k)_{k=0}^L$ of simplicial triangulations. The multigrid method relies on a Helmholtz decomposition of Nédélec's trial spaces $Nd_{1,0}(\Omega; \mathcal{T}_k)$ on all levels $0 \le k \le L$ of the hierarchy

$$Nd_{1,0}(\Omega; \mathcal{T}_k) \;:=\; Nd^0_{1,0}(\Omega; \mathcal{T}_k) \;\oplus\; Nd^1_{1,0}(\Omega; \mathcal{T}_k)$$

where $Nd^0_{1,0}(\Omega; \mathcal{T}_k)$ denotes the subspace of irrotational vector fields

$$Nd^0_{1,0}(\Omega; \mathcal{T}_k) \;:=\; \{\, \mathbf{Q}_k \in Nd_1(\Omega; \mathcal{T}_k) \;\mid\; \mathbf{curl}\, \mathbf{Q}_k = 0 \,\}$$

and $Nd^1_{1,0}(\Omega; \mathcal{T}_k)$ stands for the subspace of vector fields that are $a(\cdot,\cdot)$-orthogonal to the irrotational ones

$$Nd^1_{1,0}(\Omega; \mathcal{T}_k) \;:=\; \{\mathbf{Q}_k \in Nd_1(\Omega; \mathcal{T}_k) \mid a(\mathbf{Q}_k, \mathbf{Q}^0_k) = 0, \mathbf{Q}^0_k \in Nd^0_{1,0}(\Omega; \mathcal{T}_k)\} \;.$$

Referring to $S_{1,0}(\Omega; \mathcal{T}_k)$ as the space of continuous, piecewise linear finite elements with respect to $\mathcal{T}_k$ vanishing on Γ, any vector field $\mathbf{Q}^0_k \in Nd^0_{1,0}(\Omega; \mathcal{T}_k)$ can be uniquely represented as

$$\mathbf{Q}^0_k \;=\; \mathbf{grad}\, u_k \quad , \quad u_k \in S_{1,0}(\Omega; \mathcal{T}_k) \;\; .$$

Consequently, any vector field $\mathbf{Q}^1_k \in Nd^1_{1,0}(\Omega; \mathcal{T}_k)$ is weakly solenoidal in the sense that

$$(\mathbf{Q}^1_k, \mathrm{grad}\, v_k)_{0,\Omega} \;=\; 0 \quad , \quad v_k \in S_{1,0}(\Omega; \mathcal{T}_k) \;\; .$$

The crucial ingredient of the multigrid scheme is a distributive smoothing process consisting of a Gauss-Seidel sweep on (1.7) at levels $1 \leq k \leq L$,

$$\mathbf{S}_k \, \mathbf{A}_k \;\; = \;\; \mathbf{F}_k,$$

where $\mathbf{S}_k$ is the level k discretization matrix, followed by a Gauss-Seidel sweep on the irrotational part,

$$\mathbf{\Delta} \, \mathbf{C}_k \;\; = \;\; \mathbf{T}_k^* \, (\mathbf{F}_k \; - \; \mathbf{S}_k \, \mathbf{A}_k) \;\; .$$

Here, $\mathbf{\Delta}_k$ stands for the level k stiffness matrix associated with the FE discretization of the Laplacian with respect to $S_{1,0}(\Omega; \mathcal{T}_k)$ and $\mathbf{T}_k$ refers to the transfer operator $\mathbf{T}_k : S_{1,0}(\Omega; \mathcal{T}_k) \rightarrow Nd_{1,0}(\Omega; \mathcal{T}_k)$ given by the natural embedding $\mathbf{grad}\, S_{1,0}(\Omega; \mathcal{T}_k) \subset Nd_{1,0}(\Omega; \mathcal{T}_k)$.
For local adaptive grid refinement/coarsening we use an efficient and reliable residual-based a posteriori error estimator. This estimator relies on a Helmholtz decomposition of $H_0(\mathbf{curl}; \Omega)$ and thus enables to estimate the irrotational and weakly solenoidal part of the error separately. For details we refer to [1] and [2].

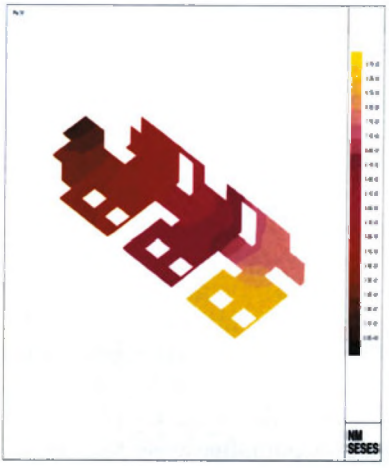

Fig. 1.2a. Electric potential

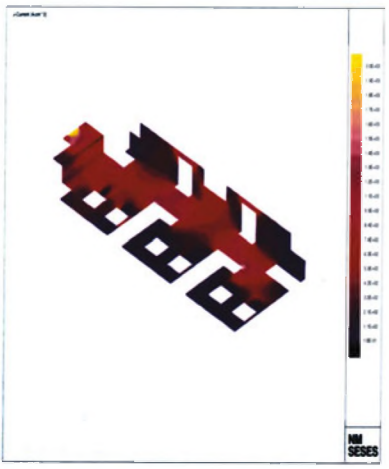

Fig. 1.2b. Electric currents

Finally, we note that the exterior domain problem can be solved by means of a boundary integral formulation using boundary elements. Here, another Helmholtz decomposition of an associated tangential trace space plays a crucial role which allows to construct appropriate preconditioners for the discretized problem. Results will be reported elsewhere.

2 Electrostatically Driven Micromembrane Pumps

Micromembrane pumps are important technological components of microfluidic systems used, for example, as implantable medical surveillance systems

for the control of metabolism such as diabetes or in the multivariable chemical analysis of fresh water bodies (cf., e.g., [12,13,15]).

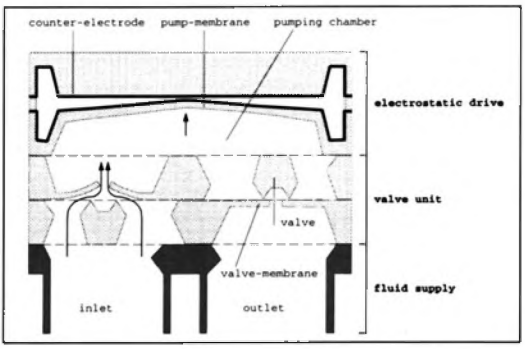

Fig. 2.1. Schematic structure of a micromembrane pump

Fig. 2.1 displays the schematic structure of an electrostatically driven micromembrane pump. The pump consists of a displacement unit, the pumping chamber with the pump-membrane, and two passive valves as well as a fluid supply. The pumping chamber measures 7mm times 7mm^2 and the thickness of the pump-membrane is about 40 μm. The operating behaviour is as follows: If voltage is applied to the contact at the upper part of the pump-membrane, the electrostatic traction on the membrane causes a deflection towards the counter-electrode leading to low pressure in the pumping chamber. The inlet valve opens and the fluid enters the chamber as long as the membrane approaches the counter-electrode. During this so-called suction phase the outlet remains closed, since the outlet valve is pushed towards the supporting structure. When the voltage is switched off, the electrostatic drive discharges by an outer circuit. The pump-membrane moves back and the thus generated high pressure in the chamber causes the fluid to leave the chamber through the outlet valve. The motion of the membrane stops as soon as a balance in the pressure is achieved. This terminates the so-called pressure phase. Both the suction and the pressure phase constitute a pumping cycle that is periodically repeated when the pump is in operating mode.

The mechanisms governing the pumping cycle are based on a subtle interaction of electrostatic, elastomechanical, and fluidmechanical forces. Thus, the mathematical modeling by continuum mechanical models leads to a coupled system of partial differential equations featuring a time-varying computational domain.

Let us first consider the model for the electrostatic displacement unit. By a phenomenological physical reasoning the electrostatic drive can be interpreted as the parallel wiring of infinitely many differentially small plate capacitors, each capacitor consisting of two horizontal parallel plates with isolation layers of width $d_{ox}/2$. Denoting by ε_0 and ε_{ox} , ε_{in} the absolute and relative permeabilities, respectively, the electrostatic traction can be expressed as a

function of the displacement u of the membrane

$$g(u) = \frac{1}{2}\epsilon_0\epsilon_{in}\left(\frac{\epsilon_{ox}U}{\epsilon_{in}d_{ox} + \epsilon_{ox}(d-u)}\right)^2 .$$

(cf., e.g., [7,15]). Then, the displacement can be obtained by the solution of a constrained minimization problem for the total energy of the membrane: Find $u \in K$ such that

$$\begin{aligned} J(u) &= \inf_{v\in K} J(v), \\ J(v) &:= \tfrac{\mu}{2}\int_\Omega \nabla v\cdot\nabla v dx - \lambda\int_\Omega \hat{g}(v)v dx \end{aligned} \tag{8}$$

where the constraint set K is of upper obstacle type $K := \{v \in H_0^1(\Omega) \mid v \leq d \quad \text{a.e.}\}$. Note that we have formally set $\lambda := U^2$ and $\hat{g}(v) := \frac{1}{2}\epsilon_0\epsilon_{in}(\epsilon_{ox}/(\epsilon_{in}d_{ox} + \epsilon_{ox}(d-v))^2$.
The optimality conditions give rise to a nonlinear complementarity problem: Find $u \in H_0^1(\Omega) \cap H^2(\Omega)$ such that

$$\begin{aligned} -\mu\Delta u - \lambda f(u) \leq 0 \ , \ u - d \leq 0 \quad \text{a.e. in } \Omega \\ (-\mu\Delta u - \lambda f(u), u-d)_{0;\Omega} = 0 \ . \end{aligned} \tag{9}$$

It is well known that such problems are characterized by the occurrence of multiple solutions. Apart from primary and secondary bifurcations, alone the main solution branch may exhibit a variety of right- and left-turning fold points (cf., e.g., [5,8]).
A standard approach for the computation of the solution branch relies on path-following continuation strategies (cf., e.g., [11]). Here, following [8] we use the potential energy $\sigma := a(\cdot,\cdot)^{1/2}$ as the continuation parameter. In particular, denoting by $C := \{x \in \Omega \mid u(x) = d\}$ the contact set, we may split the potential energy according to

$$a(u,u) = \mu \int_C |\nabla u|^2 \, dx + \mu \int_{\Omega\setminus C} |\nabla u|^2 \, dx = a_C(u,u) + \lambda\, b_C(u) \ ,$$

$$a_C(u,u) := \mu \int_C |\nabla u|^2 \, dx \quad , \quad b_C(u) := \int_{\Omega\setminus C} f(u)\, u \, dx$$

where we have taken into account that on $\Omega \setminus C$ we have equilibrium, i.e., $-\mu\,\Delta\, u = f(u)$. This leads to the augmented nonlinear complementarity system

$$\max\,(\, -\mu\,\Delta\, u \,-\, \lambda\, f(u)\,,\, u \,-\, d\,) = 0 \qquad \text{on} \quad \Omega \ , \tag{10}$$

$$\sigma^2 \,-\, [\, a_C(u,u) \,+\, \lambda\, b_C(u)\,] = 0 \ . \tag{11}$$

The path-following continuation strategy is realized by a nonlinear multigrid predictor-corrector technique based on a standard conforming P1 finite

element approximation of (2.3),(2.4) with respect to a hierarchy $(\mathcal{T}_k)_{k=0}^{L}$ of simplicial triangulations.
In particular, on the lowest level $k = 0$ the predictor features an explicit Euler step based on an arc-length parametrization of the solution branch whereas on the higher levels $1 \leq k \leq L$, nested iteration is performed using mimicked Euler prediction in terms of prolongated secants as startiterates for nonlinear multigrid V-cycles involving levels 0 up to k. The multigrid cycles are the same used in the corrector step which relies on nonlinear multigrid techniques. In particular, both as a smoother and as an iterative solver on the coarsest grid we have chosen projected Gauss-Seidel-Newton iteration followed by a λ-update according to (2.4). The coarse grid correction is constructed following the so-called FAS technique (Full Approximation Scheme, cf. [4,6]) in order to guarantee that the coarse grid correction on level $k-1$ does provide an approximation on the same solution branch. For details we refer to [7].

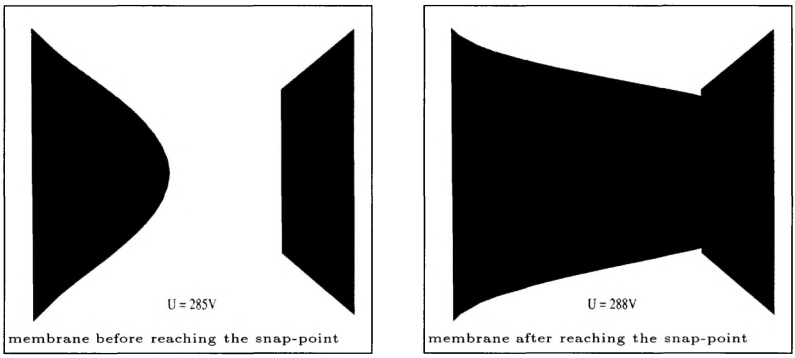

Fig. 2.2a. Deflection of the membrane

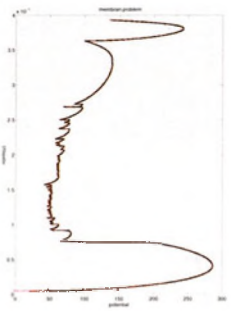

Fig. 2.2b. Bifurcation diagram

Fig. 2.2a displays the deflected membrane before and after the so-called snap-point which corresponds to that state where we will still have equi-

librium of the potential and the electrostatic energy and thus no contact with the counter-electrode. After reaching the snap-point, the electrostatic energy dominates and the membrane snaps through being in contact with the counter-electrode. In the bifurcation diagram (cf. Fig. 2.2b), the snap-point corresponds to the first left-turning fold point which indicates the transition from the stable to the unstable part of the main solution branch.
The fluid-structure interaction between the motion of the fluid and the deflection of the valves can be modeled by a coupled system of initial-boundary-value problems for the incompressible Navier-Stokes equation in the pumping chamber and the elastic beam equation for the valves, respectively:

$$\frac{\partial \mathbf{u}}{\partial t} + (\mathbf{u} \cdot \nabla)\mathbf{u} - \nu \Delta \mathbf{u} + \nabla p = 0 \text{ in } \Omega \times (0,T), \tag{12}$$

$$\mathbf{u}(\cdot,0) = \mathbf{u}^0 \quad \text{in } \Omega \ , \quad \mathbf{u} = \mathbf{g} \quad \text{on } \Gamma_D \times (0,T) \ , \tag{13}$$

$$-p + \nu \frac{\partial \mathbf{u}_n}{\partial \mathbf{n}} = P, \quad \frac{\partial \mathbf{u}_t}{\partial \mathbf{n}} = 0 \text{ on } \Gamma_N \times (0,T). \tag{14}$$

Here, $\mathbf{u}$ and p denote the velocity field and the pressure in the pumping chamber Ω whose boundary Γ is split into $\Gamma = \Gamma_D \cup \Gamma_N$, $\Gamma_D \cap \Gamma_N = \emptyset$, where Γ_N stands for the part occupied by the valves. $\mathbf{u}_n$ and $\mathbf{u}_t$ are the normal and tangential components of the velocity on Γ_N. Finally, the vector-valued functions $\mathbf{u}^0$, $\mathbf{g}$, the scalar function P, and the constant ν refer to the initial velocity at time $t = 0$, the prescribed velocity on Γ_D, the prescribed pressure on Γ_N, and the kinematic viscosity, respectively.
The initial-boundary-value problem for the elastic beam describing the deflection of a valve of length L being clamped at its left end is as follows.

$$\rho Q \frac{\partial^2 y}{\partial t^2} + EJ \frac{\partial^4 y}{\partial x^4} = f \quad \text{in} \quad (0,L) \times (0,T] \ , \tag{15}$$

$$y(\cdot\,,0) = 0 \qquad \text{in} \quad [0,L] \ , \tag{16}$$

$$\begin{aligned} y(0,t) = y''(0,t) = 0, \\ y'(L,t) = y'''(L,t) = 0, \quad t \in (0,T) \end{aligned} \tag{17}$$

where ρ is the density, Q the transversal force, E the elasticity module, J the moment of inertia, and f the applied load.
For the numerical solution of the Navier-Stokes equations, the programme package FEATFLOW [14] has been used relying on an automatic time-stepping based on implicit discretizations in time and an adaptive nonconforming finite element discretization in space with respect to quadrilateral

triangulations of the computational domain. The beam equation has been solved by the backward Euler scheme in time and piecewise cubic Hermitian polynomials in space. The fluid-structure interaction has been realized by an outer iteration featuring the solution of the beam equation, the actualization of the computational domain for the flow field, the boundary conditions, and an adaptation of the quadrilateral triangulation, as well as the solution of the Navier-Stokes equations.

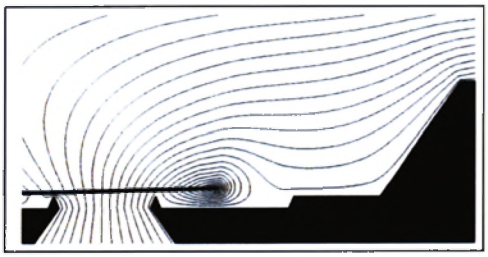

Fig. 2.3a. Streamlines (pressure phase)

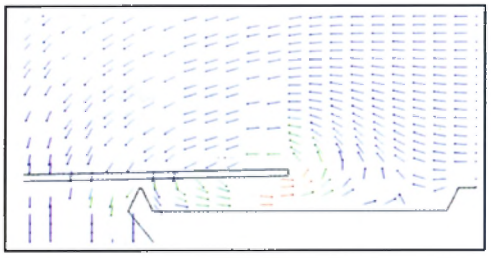

Fig. 2.3b. Flow field (pressure phase)

Fig.s2.3a-b illustrate the computed streamlines and the flow field in a vicinity of the inlet valve during the pressure phase of the pumping cycle.

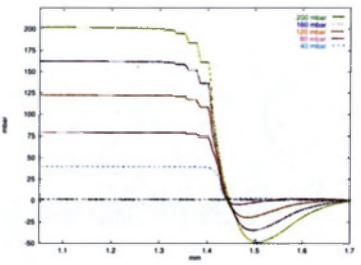

Fig. 2.4a. Pressure difference (inlet valve)

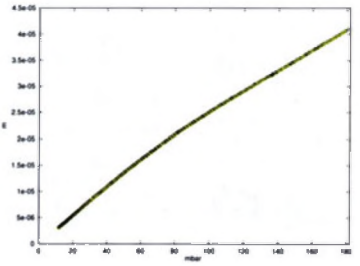

Fig. 2.4b. Displacement (inlet valve)

Finally, Fig.2.4a shows the distribution of the difference in the pressure at the inlet valve for various (constant) pressures at the supplies whereas Fig. 2.4b displays the displacement of the inlet valve (distance from the supporting structure) as a function of the pressure.

3 Micromachined Deformable Bimorphic Mirrors

Silicon integrated-circuit fabrication technology has been used to develop small deformable mirrors with electrostatic actuators for the effective control of the mirror shape. Such micromachined mirrors have potential applications in adaptive optical systems as, for instance, in the positioning of laser beams in optical eye surgery.

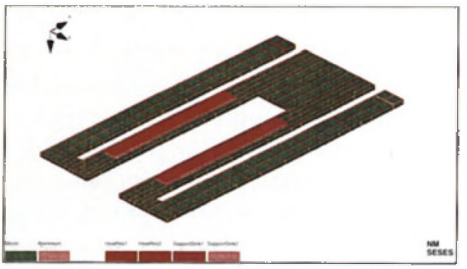

Fig. 3.1. Bimorphic mirror

Fig.3.1 displays a bimorphic micromirror with a springboard-like shape whose length and width are approximately 800 and 500 μm compared to a thickness of about 20 μm. The mirror is equipped with two aluminum contacts.
The functioning of the mirror is as follows: The alu-contacts are electrically heated which causes a mechanical deformation due to the bimorphic character of the device. The purpose is to apply the operating voltage in such a way that a sensitive control of the mirror deformation can be achieved.
In the following we will concentrate on the computation of the transient

behavior of the temperature and the heat flow of the mirror which can be obtained by a heat equation with discontinuous coefficients, since the functions describing the density, the heat capacity, and the heat conductivity exhibit jumps at the interfaces between the silicon and the aluminum. The heating is modelled by time-periodic Neumann boundary data at the alu-contacts whereas we have homogeneous Dirichlet resp. homogeneous Neumann boundary conditions elsewhere.

$$\begin{array}{l} \rho\, c\, \frac{\partial \Theta(x,t)}{\partial t} \; - \; div(\lambda\, grad\, \Theta(x,t)) \; = \; 0 \;\; , \\ (x,t) \in \Omega \times (0,T) \end{array} \tag{18}$$

where ρ stands for the density and c and λ refer to the heat capacity and heat conductivity, respectively.

a) Homogeneous Dirichlet data at SuppSink1/2

$$\Theta(\cdot,t) \; = \; 0 \quad on \quad \Gamma_S \tag{19}$$

b) Time-periodic Neumann data at alu-contacts

$$\lambda\, n \cdot grad\, \Theta(\cdot,t) \; = \; \left\{ \begin{array}{l} k\, sin^2(10^5 \pi t) \\ k\, cos^2(10^5 \pi t) \end{array} \right\} \; on \; \left\{ \begin{array}{l} \Gamma_{H_1} \\ \Gamma_{H_2} \end{array} \right\} \tag{20}$$

c) Homogeneous Neumann data elsewhere

$$\begin{array}{l} \lambda\, n \cdot grad\, \Theta(\cdot,t) \; = \; 0 \quad on \\ \Gamma_{Nat} := \Gamma \setminus (\Gamma_S \cup \Gamma_{H_1} \cup \Gamma_{H_2}) \end{array} \tag{21}$$

For the efficient numerical simulation we have implemented a solution process that allows for the simultaneous computation of the temperature and the heat flow and whose main feature is a combined automatic time-step selection and adaptivity in space. For that purpose, the spatial discretization has been done using primal mixed finite elements with respect to hexahedral triangulations of the computational domain. This approach is based on the primal mixed variational formulation of the problem that can be obtained by introducing the flux $\mathbf{j}$ as an additional unknown. We note that in contrast to the dual mixed approach the relationship between the primal and the dual variable is considered in the strong L^2-sense whereas the semi-discretized heat equation is treated in its weak sense.

The mixed discretization leads to an algebraic saddle point problem with a 2×2 block coefficient matrix whose first diagonal entry is block-diagonal and hence easily invertible. Static condensation of the discrete flux results in a Schur complement system that is solved by preconditioned conjugate gradients.

An adaptive grid adaptation can be realized in various ways as, for example, by a hierarchical type a posteriori error estimator where the equation satisfied by the total error is discretized using higher order ansatz spaces combined with their hierarchical two-level splitting in order to provide an appropriate

localization. For automatic time-stepping we have followed the approach due to Bornemann [3] where the heat equation is considered as an evolution equation in Hilbert space which allows to apply extrapolation techniques known from the numerical solution of ODEs. The discretization in space is treated as a perturbation of the extrapolation tableau. With respect to a prespecified tolerance and a safety factor this gives rise to a prediction of the new time-step.

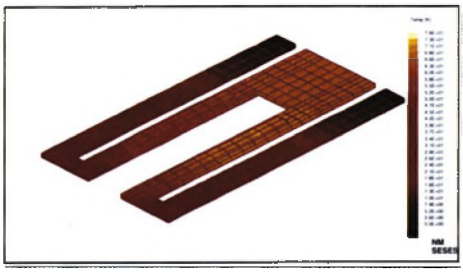

Fig. 3.2a. Temperature at time $t = \frac{2}{k}$

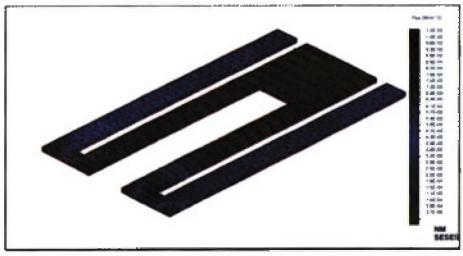

Fig. 3.2b. Heat flow at time $t = \frac{2}{k}$

The above features have been implemented within the programme package NM SESES. Fig.s3.2a-b show the computed temperature and heat flow at some time $t = \frac{2}{k}$.

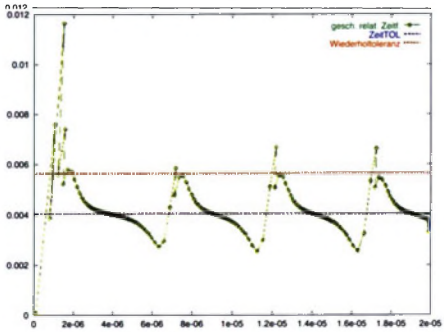

Fig. 3.3a. Relative estimated error

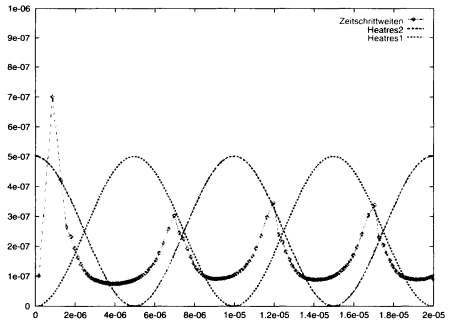

Fig. 3.3b. Effective time-steps

The performance of the error estimator is displayed in Figs. 3.3a–b. In particular, Fig. 3.3a shows the temporal history of the relative estimated error with respect to the prespecified tolerance which is shown as the dotted line. Only those time-steps where the error was above that line had to be repeated which – in this example – were 6 time-steps compared to a total of 157 time-steps being thus less than 4 %.
Fig. 3.3b illustrates the temporal history of the effective time-steps together with the scaled time-periodic Neumann boundary data at the alu-contacts. We clearly observe the periodic behavior after a short start-up phase.

References

1. Beck, R., Deuflhard, P., Hiptmair, R., Hoppe, R. H. W., Wohlmut, B.: Adaptive multilevel methods for edge element discretizations of Maxwell's equations. To appear in Surveys of Math. in Industry, 1998
2. Beck, R., Hiptmair, R., Hoppe, R. H. W., Wohlmut, B.: Residual-based a posteriori error estimators for curl-conforming finite element approximations. To be submitted to Math. Model. Anal. Numer.
3. Bornemann, F. A.: An adaptive multilevel approach to parabolic problems in two space dimensions. Dissertation, Freie Universität Berlin, 1991
4. Brandt, A.: Multi-level adaptive solutions of boundary-value problems. Math. Comput. **31**, 333–390 (1977)
5. Conrad, F., Issard-Roche, F., Brauner, C.-M., Nikolaenko, B.: Nonlinear eigenvalue problems in elliptic variational inequalities: A local study. Comm. Partial Differential Equations **10**, 151–190, 1985
6. Hackbusch, W.: Multi-Grid Methods and Applications. Springer, Berlin-Heidelberg-New York, 1982
7. Hoppe, R. H. W., Sieber, E. R., Wachutka, G., Wiest, U.: Mathematical modelling and numerical simulation of a free boundary problem for an electromechanical micropump. An. St. Univ. Ovidius Constanta, Vol. 5(1), 65–78, 1996
8. Hoppe, R. H. W., Mittelmann, H. D.: A multi-grid continuation strategy for parameter-dependent variational inequalities. J. Comput. Appl. Math. **26**, 35–46 (1989)

9. Kühn, F.: Volladaptive Finite-Elemente-Verfahren in der Simulation instationärer elektrothermischer Effekte in mikromechanischen Bauteilen. Diplomarbeit, Universität Augsburg, 1997
10. Nédélec, J.: Mixed finite elements in $\mathbf{R}^3$. Numer. Math. **35**, 315–341 (1980)
11. Rheinboldt, W. C.: Numerical Analysis of Parametrized Nonlinear Equations. John Wiley & Sons, New York, 1986
12. van de Schoot, B. H., Jaenneret, S., van den Berg, A., de Roji, N. F.: Modular setup for a miniaturized chemical analysis system. Sensors & Actuators **B 15–16**, 211–213 (1993)
13. Shoji, S., Nakagawa, S., Esashi, M.: Micropump and sample-injector for integrated chemical analyzing systems. Sensors & Actuators **A 41–42**, 189–192 (1990)
14. Turek, S.: FEATFLOW. Finite element software for the incompressible Navier-Stokes equations: User Manual, Release 1.0. University of Heidelberg, 1995
15. Zengerle, R.: Mikro-Membranpumpen als Komponenten für Mikro-Fluidsysteme. Dissertation, Universität der Bundeswehr München, 1994